CrossMark

Leveraging Full-Field Measurement from 3D Digital Image Correlation for Structural Identification

M. Shafiei Dizaji [1] · M. Alipour [1] · D. K. Harris [1]

Abstract

Within the domain of structural health monitoring (SHM) measurement techniques have primarily relied on discrete sensing strategies using sensors physically attached to the structural system of interest. These sensors have proven effective in describing both global and local phenomena, but are limited to providing discrete response measurements of these systems. With the introduction of novel imaging tools and image analysis techniques, such as digital image correlation (DIC), the ability to measure the full-field response of these systems provides a novel approach to refining structural identification (St-ID) approaches used in SHM. This paper explores this proposed concept through a case study on a series of structural test specimens analyzed using 3D digital image correlation (3D-DIC) for St-ID. Finite element model updating (FEMU) was used as the technique for the structural identification. For the identification process, ABAQUS was interfaced with MATLAB to converge on the optimal unknown/ uncertain system parameters of the experimental setup. 3D-DIC results provided a rich full-field dataset for the identification process, which was compared against measurements derived from traditional physical in-place sensors typically used in SHM. In this work a Hybrid Genetic Algorithm (HGA), which combines the genetic algorithm as a global optimization and a gradient-based method as a local optimization, was used for the FEMU based on 3D-DIC results of structural specimen subjected to variable loading. To minimize the error between the full field 3D-DIC measurements and FEA model updating results, an objective function was introduced that included the full-field contributions of strains and deformation response. The evolution of this objective function illustrated satisfactory convergence of the identified parameters and the excellent agreement of the experimental and numerical strain and displacement responses after the model updating process confirmed the success of the proposed approach. The results of this study highlight the advantage of this hybrid approach and provide the foundation for effective deployment of the proposed strategy for large-scale structural systems.

Introduction

Much of the physical infrastructure across the globe was built during eras of growth and with a finite intended service life, but in many cases these systems have continued to operate and

✉ M. Shafiei Dizaji
  ms4qg@virginia.edu

  M. Alipour
  ma4cp@virginia.edu

  D. K. Harris
  dharris@virginia.edu

1 University of Virginia, 351 McCormick Rd,
  Charlottesville, VA 22904, USA

have remained in service well beyond this intended period [1]. Infrastructure owners and managing entities have proven capable of keeping these systems functional through routine and preventative maintenance strategies, but often these strategies are reactive in nature and are deployed in response to an observable deterioration mechanism. However, recent structural failures have demonstrated that this approach is not always effective and can have catastrophic and even fatal consequences [2, 3]. The concept of structural health monitoring (SHM) has shown promise as a strategy for temporal condition assessment of the built environment. SHM provides a system performance evaluation strategy with the end goal of characterizing behavior and providing indications of damage and even forewarning of impending failure.

The concept of SHM has existed for several years in various forms across multiple engineering disciplines [4] and has

been likened to a human health management system [5], with well-person checkups, preventative intervention, and treatment/surgery being analogized to inspection, maintenance, and repair/retrofit, respectively. The body of knowledge in SHM has grown considerably over the past few decades, but a fundamental challenge that remains is the translation of measurable phenomena derived from full-scale physical systems into information that describes the system's health and condition. To date, significant research has been performed on condition assessment [6, 7] and SHM [8] of infrastructure with advances in novel technologies [9–11] and assessment techniques [12, 13]. However, a comprehensive solution also requires integrated strategies for routine inspection, data management, result interpretation and decision support, demonstrating that SHM is still in its infancy with excellent opportunities for growth and development. As society pushes towards a more holistic strategy of smart and connected communities, the need for low cost, non-invasive, and data rich techniques is becoming paramount to the SHM community. This manuscript describes an experimental study that aims to address this challenge by leveraging digital image correlation (DIC) for structural identification (St-ID) within the SHM framework as a strategy of collecting rich, full-field data without the need for fixed in place sensors. With the challenges associated with an aging infrastructure network [10–13], non-invasive tools such as DIC have the potential to provide decision-makers with a comprehensive assessment tool to better describe the performance of this network.

This paper presents an experimental study that leverages three-dimensional digital image correlation (3D-DIC) as a full-field measurement approach within the broader SHM framework. A synthesis of the findings of this study are presented and organized as follows: first, a strategy for full-field structural identification within the SHM framework is investigated. Next, the experimental setup along with the 3D-DIC configuration is described including the testing objectives and key DIC parameters. A description of the ground truth measurements collected from traditional affixed sensors is also presented. Finally, the preliminary modeling approach using the finite element method is described. Leveraging results from the 3D-DIC measurements, a structural identification optimization using the preliminary finite element model updated with full-field 3D-DIC results to converge on boundary and constitutive properties of the test specimen. Critical to this updating process was the concept of interpolation between DIC results and FEA results, and optimization process, which is described in detail. Finally, a discussion of the results and conclusions are presented.

Structural Identification Within SHM Framework

Within the traditional SHM framework, numerical models, typically finite element models (FEM), are commonly used to describe the behavior of structural systems. FEM has been used with great success to simulate structural response of idealized systems, but its approximate nature and simplifying assumptions coupled with uncertainties associated with boundary conditions and condition inherently result in errors when describing existing structural systems [14]. Structural identification (St-ID) describes an approach that emphasizes correlation of the response characteristics between a model and experiment, providing a basis for using an updated FE model to characterize critical performance measures of existing structural systems. Within St-ID, this inverse problem aims to minimize differences between analytical and experimental results and is usually formulated as an optimization problem. Satisfactory correlation between the observed experimental behavior and the analytical results is critical, but equally essential is maintaining the physical significance of updated parameters [15]. For this purpose, setting up of an objective or cost function and selecting updating parameters are crucial steps in St-ID. The changes in these parameters are then determined iteratively and pushed to a minimum via an optimization algorithm. St-Id aims to bridge the gap between the model and the real system by developing reliable estimates of the performance and vulnerability through improved simulations. This work describes an experimental case study that leverages 3D digital image correlation (3D-DIC) for St-ID.

Three dimensional DIC (3D-DIC) leverages calibrated stereo-paired cameras to enable 3D imaging, allowing for shape and out-of-plane surface deformations to be measured. A comprehensive treatment of DIC is available in the literature [16–31] and not presented here, but additional details on the DIC deployment used in this investigation are provided in a later section. An interesting characteristic of DIC is that the representation of full-field surface deformations is analogous to results derived from FEA, creating the potential for full-field structural identification, a capability that is not possible with discrete sensors. Figure 1 provides a generalized illustration of the proposed St-ID strategy used in this investigation, which will be described in more depth in the following sections.

Generally, for St-ID, a cost function, defined in terms of differences between numerical and experimental displacement fields, is minimized on part of the system boundary in an iterative manner by changing the material parameters and boundary conditions. Given a unique set of system geometry, material parameters, traction and displacement boundary conditions, the displacement and deformation response of a system is also unique. Hence, assuming the system geometry and boundary conditions are correctly replicated in the Finite Element (FE) model, convergence between numerical and experimental displacement fields is achieved only when the constitutive parameters approach their true values. Examples of this optimization concept
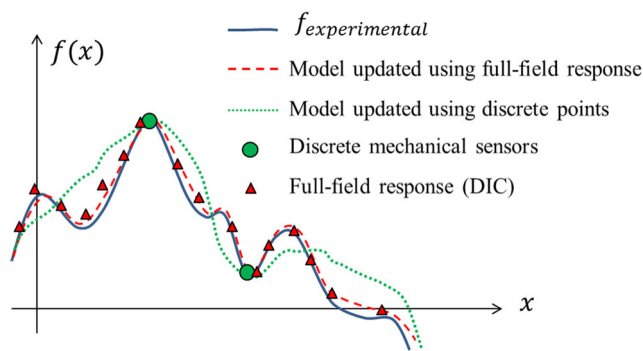
Fig. 1 Overview of the proposed full-field St-ID process
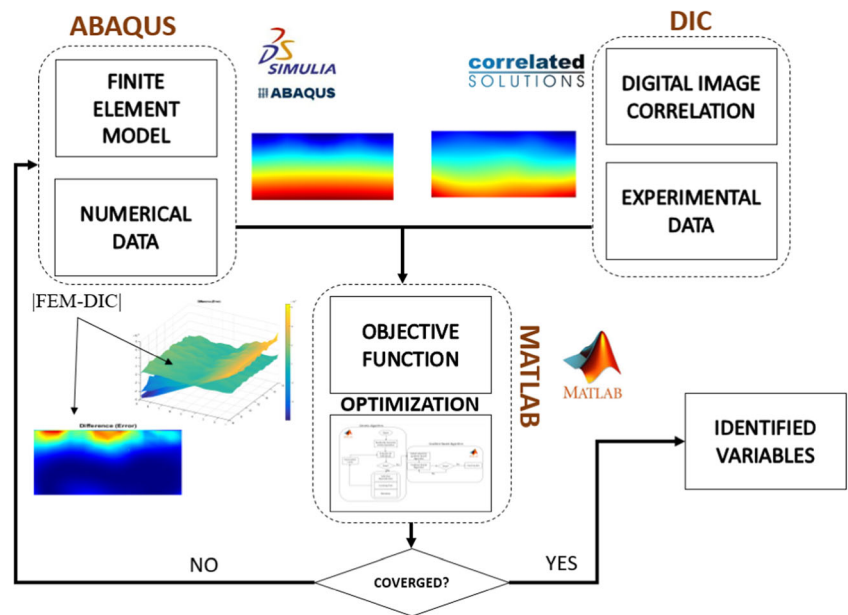
are available across numerous fields, but representative St-ID examples are available in [32–36].

This work explores a new vision-based structural identification (St-ID) framework that allows for full-field structural behavior matching and identification and can result in significant enhancements compared with the use of traditional discrete-point mechanical sensors that are typically used in current SHM and St-ID applications. Figure 2 conceptualizes the potential advantage of the proposed framework for model updating and St-ID using full-field response measurements (i.e. 3D-DIC) in comparison with those obtained by discrete point sensors (e.g. strain gages, LVDTs, etc.). The dotted line depicts the predictions of an FEM model updated by matching measurements of only two discrete mechanical sensors. The dashed line is a model updated using a fine grid of points on a full-field response measurement. In this illustration, it becomes evident that matching a complex function using a limited set of discrete mechanical sensors may result in good agreement in the proximity of the sensors, but does not guarantee a good match in other locations on the specimen. On the other hand, matching an entire full-field response enables a more comprehensive representation of the global and local behaviors throughout the specimen. This advantage is expected to be realized in more complex structural systems, where only a few discrete points may be insufficient to describe the behavior. An example is a structure with geometrical non-uniformities (e.g. a hole or defect) or complicated boundary conditions where the response cannot be uniquely represented by a few discrete sensors.

Experimental Study and Numerical Simulation

For a proof of concept to the proposed full-field St-ID framework, an experimental study was performed. The experimental specimen examined in this work is a relatively simple structural system and the work presented in this paper include a series of laboratory and corresponding numerical model case studies that provide the foundation for expanding this concept. Future works by the authors aim to illustrate these advantages in more complex structural systems such as full-scale highway bridge structures.

Experimental Setup

In this investigation, an experimental program was developed to evaluate the feasibility of leveraging 3D-DIC in a St-ID/SHM framework. The experimental program included a laboratory scale investigation of a representative steel beam subjected to various loading and boundary conditions. The structural configurations used in this investigation are illustrated schematically in Fig. 3 and can be described as:


Fig. 2 FEA model updating using discrete sensors versus full-field response

1) Configuration 1 (*CF1*): structural component simply supported (Cylinder) subjected to concentrated load at midspan (Fig. 3(a)).
2) Configuration 2 (*CF2*): structural component simply supported (Half Cylinder) subjected to concentrated load at midspan (Fig. 3(b)).
3) Configuration 3 (*CF3*): structural component with simple and partial support restraints subjected to a concentrated load at midspan (Fig. 3(c)).

The restraint configurations illustrated in Fig. 3 were intended to mimic idealized boundary and loading conditions and provide a basis for characterizing the differences these idealized conditions and real systems. Figure 4 shows the actual boundary and loading fixtures used in experimental set up for different configurations.

The testing program consisted of a series of flexural loading cycles within the elastic range (σ_{yield}= 50 ksi) on a wide-flange hot-rolled structural steel beam (ASTM A992 W10x22). The 172 in. beam was tested in the Structures Laboratory at the University of Virginia and configured for strong-axis bending. The beam was instrumented with Bridge Diagnostic Inc. (BDI) sensors at both midspan and support locations to provide a comparison between traditional SHM sensor results and those derived from the 3D-DIC measurements (Correlated Solutions *VIC-3D*) at the same locations. Three paired DIC camera (Point Grey Grasshopper 2.0 CCD with 5.0MP resolution) systems were used to evaluate the midspan (Schneider 8 mm lens) and two end span (Schneider 12 mm lenses) locations. The midspan camera system utilized a different lens configuration due to the physical constraints of the load frame location relative to the test specimen. The end and midspan locations were patterned over the full depth of the beam web over 24 in. with the pattern created by applying a flat white paint base coat, followed by random speckle pattern with a permanent marker. Additional details on the pattern and camera setup are provided in a later section. The DIC data acquisition (DAQ) integrated output signals (load and displacement) from MTS actuators and controller to allow for simultaneous acquisition of load, displacement, and images. The BDI DAQ system was not directly linked, but was synchronized manually at the start of each test. Figure 5(a) provides a basic illustration of the experimental setup and instrumentation configuration used during testing.
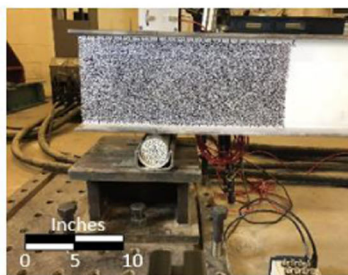
Fig. 3 Schematic of the steel beam loading and boundary conditions used during experimental testing (**a**) Configuration 1 (**b**) Configuration 2 (**c**) Configuration 3
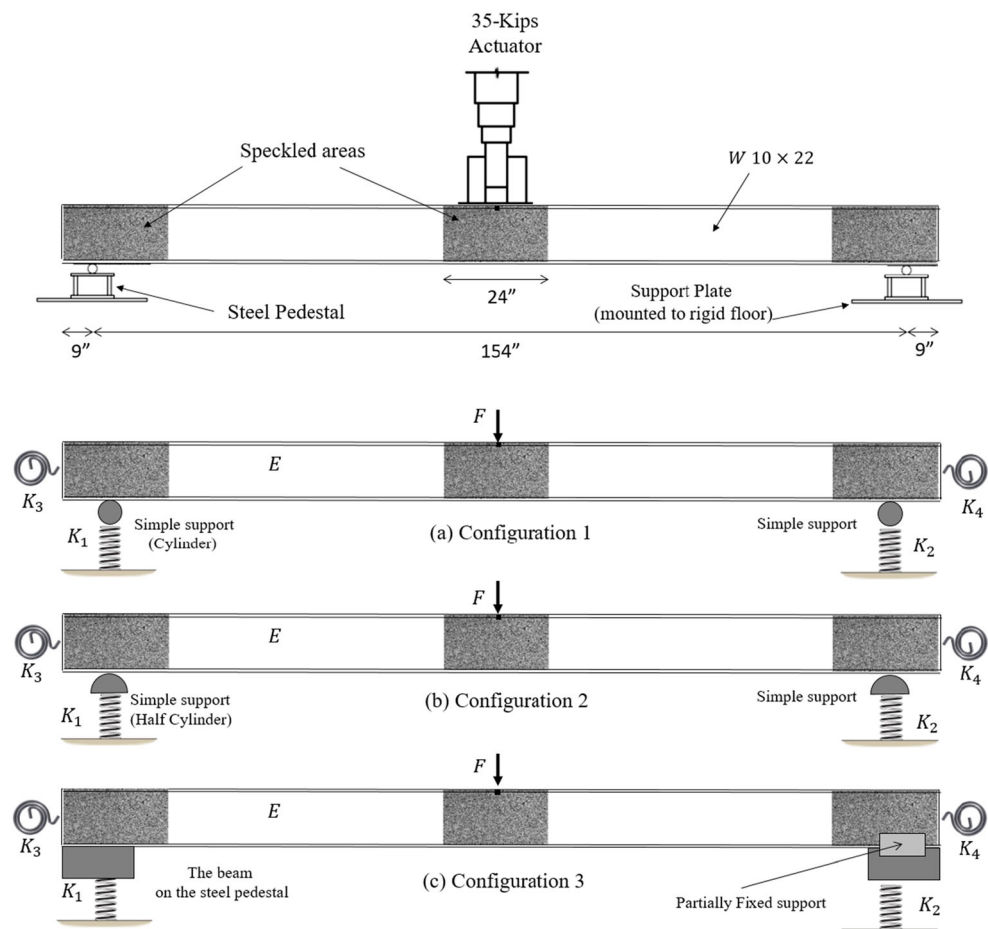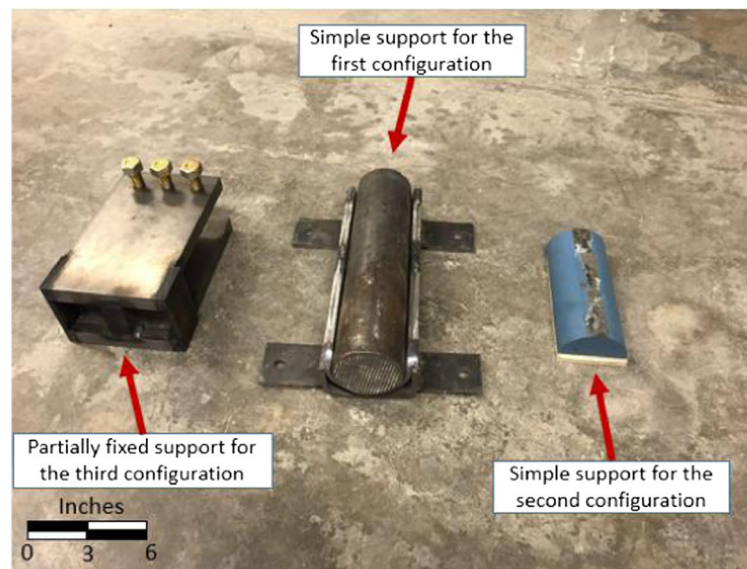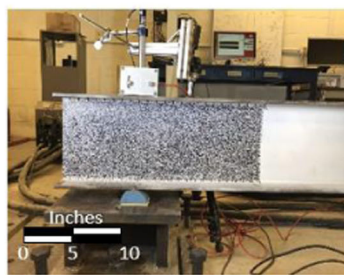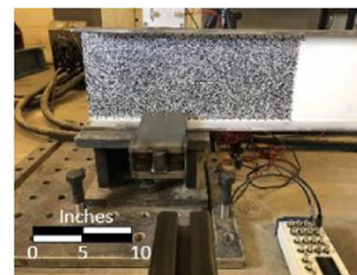
Fig. 4 Boundary and loading fixtures (**a**) different supports used in the tested configurations (**b**) supports used for the first configuration (**c**) supports used for the second configuration (**d**) support used for the third configuration

Loading regime

For each of the configurations, the beam was loaded monotonically under displacement-control, with the beam response maintained within the elastic range. The loading sequence consisted of loading the beam to a displacement of 0.05 in. at a rate of 0.002 in. per second, followed by a two-cycle sinusoidal loading from 0.05 in. up to a peak displacement of 0.3 in., and concluding with an unloading through the reverse of the initial loading sequence. The initial loading and final unloading occurred over a period of 50 s (25 s each), while the sinusoidal sequence occurred over a period of 500 s (250 s for each cycle). The BDI DAQ collected data during the loading sequence at 100 Hz while the DIC images were acquired at 2 Hz which resulted in 1143 images.

DIC setup

As previously noted, the DIC image acquisition used three sets of stereo-paired digital cameras. Each camera had a 5-megapixel charge coupled device (CCD) image sensor with a resolution of 2448 × 2048. The image sensor for this camera was 2/3″ format with dimensions of 0.35″ × 0.26″, which accounted for a pixel size of 1.36×10^{-4} in.. The camera was connected to a C-mount optical lens and the acquired data was communicated to the control PC through FireWire cables. To accommodate the specimen within the field of view of cameras with the highest resolution, the design on the imaging setup was achieved by considering the geometrical restraints of the laboratory space (maximum available space from cameras to the beam was about 50 in.) as well as the available optical lenses. Using 12 mm lenses for the end locations and 8 mm lenses for the middle location, the distance of the camera from the beam was calculated using equation (1), where w/h is the sensor width/height, W/H is the field of view width/height, d is the distance to the object, and f is the focal length (Fig. 5(b) (Left)). Using the dimensions of the speckled region (24″ × 9.5″) and leaving a space of at least 1 in around each side of the region to accommodate deformations to be

Fig. 5 Experimental setup and camera configuration (**a**) 6 camera setup (3 systems or 3 camera pairs) 1 pair at midspan (8 mm lens) and 1 pair at each support (12 mm lens) (**b**) Diagram of the optical setup (Left), Field of view, speckle pattern and subsets (Right)
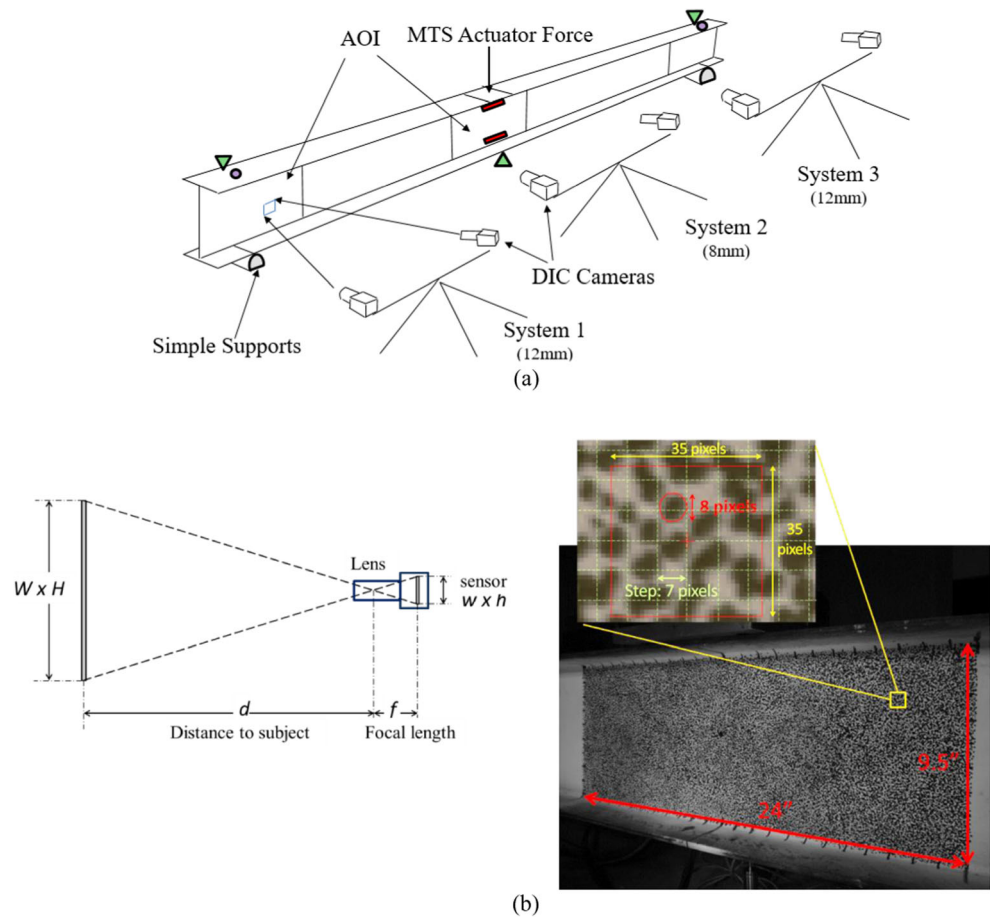

captured, the 8 mm and 12 mm lenses had to be placed at about 23.5″ and 35″ from the specimen (Fig. 5(b) (Right)), respectively, to produce the same field of view.

$$\frac{w}{W} = \frac{h}{H} = \frac{f}{d} \qquad (1)$$

In preparation for testing, the surface of the test specimen was covered with a fine, dense and random speckle pattern for the correlation process. To achieve a high spatial resolution of calculated results while at the same time being large enough to be resolved in the images, the pattern had an average speckle size of 0.08 in., which corresponds to approximately 8 pixels in the captured images. For the pixel tracking process in DIC, the area of interest on the speckle pattern is split into rectangular windows or "subsets" and unique patterns of speckles need to be available within each subset to allow for tracking in subsequent frames. The patterns in the subsets is tracked on a grid of a specific "step" size, which dictates the spatial resolution of the calculated points. To achieve a fine grid of unique patterns in subsets, the selection of the subset size was achieved through direct experimentation and a square subset of 35 pixels at a step of 7 pixels was selected (Fig. 5(b) (Right)).

Numerical Simulation

As previously noted, St-ID requires the development of an initial numerical model that can be updated based on experimentally derived results. In this investigation, finite element models of each loading/boundary condition scenario were developed in ABAQUS, a robust commercially available finite element software package. For each scenario, the steel beam was modeled using a total of 4300 Continuum 3D hexahedral solid elements (C3D8) with full integration. The geometry was developed from standard section properties available within the AISC Manual of Steel Construction [37]. The boundary supports were modeled as a series of springs (translational and rotational) to represent the deviation from ideal simple and fixed conditions and to allow for updating based on experimental measurements. A global view of the model of the steel beam has been shown in Fig. 6. With the model representing a relatively non-complex structural component, a dense mesh was not required; however, the mesh density was initially developed and later refined to allow for alignment with the coordinate system of the DIC results. It should be noted that ABAQUS allowed for the development of a direct interface with MATLAB, a
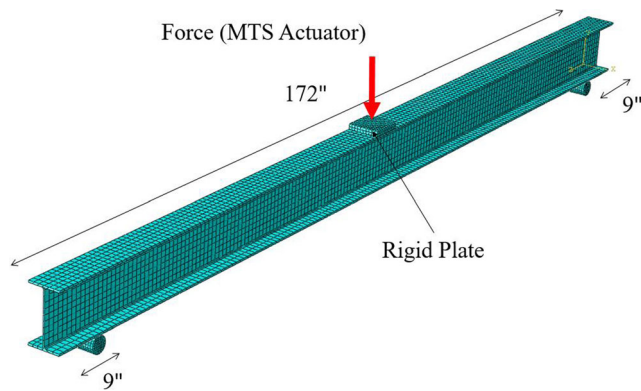
Fig. 6 Isometric view of representative finite element model of the steel beam (Configuration 1 shown)

multi-paradigm numerical computing environment, which facilitated the iterative parameter optimization algorithm.

Results and Discussion

Measurement Noise

Prior to utilizing the DIC results in the St-ID framework, an analysis of the measurement noise was performed. To evaluate the noise in the measurements, a series of images were taken from the zero-load state of the specimen and processed using the same settings used for the rest of the data. While in theory the displacements and strains should be equal to zero in the zero-load state, in practice, noise from different sources affect the measurements. Some of these sources include lighting fluctuations and glare, irregularities and poor quality of speckle pattern, as well as noise resulting from image acquisition (e.g. sensor noise) and quantization [16]. Table 1, summarizes the average and standard deviation of the displacement (U, V, W) and strain (ε_{xx}, ε_{yy}, ε_{xy}) measurements in 10 frames with zero load. The standard deviation of the measurements quantifies the variation of the noise and can be used as an estimate of the resolution of the measurements [38]. To better see the distribution of noise in zero-load frames, Fig. 7, illustrates histograms of the non-zero displacements and strains in a sample zero-load frame. It is notable that all of the no-load frames have a similar shape with a mean close to zero and a

Table 1 Noise statistics from measurements in 10 frames with zero load at midspan

Variable		Mean	StD
U	(1/1000 in.)	−0.14	0.83
V		−0.50	0.99
W		−0.18	1.44
ε_{xx}	($\mu\varepsilon$)	1.80	63.02
ε_{yy}		0.96	86.67
ε_{xy}		−0.72	60.12

bell-shaped distribution which is in agreement with the expected random Gaussian noise.

DIC Results Versus Reference Sensors

Results from the experimental program provided a basis for comparison of the 3D-DIC measurements with the in-place mechanical sensors that are representative of those used in traditional structural testing and SHM applications. For comparison, a virtual gauge was selected in the DIC system to allow for local strains to be measured within both the tension and compression regions of the cross-section as shown in Fig. 8. The evolution of strains (ε_{xx}) at the two locations, A and B (Fig. 8), along with the corresponding vertical deflection were extracted from the DIC results. Similarly, results from the support locations were extracted from the DIC; however, for this location, only displacements were considered as the strains near the supports are relatively low. Figure 9 illustrates a comparison of the results of selected sensors for one of the experiments relative to corresponding BDI sensors. Also, differences between BDI sensors and DIC are quantified in the Table 2. The results demonstrate that the measurement derived from both systems are comparable, but the DIC results exhibit a noisier response. This outcome is expected, but it should also be noted that the full-field measurement capability derived from DIC cannot be achieved with local sensing techniques and the full-field measurement provides a unique capability for a more robust St-ID strategy. During the experiments, the DIC measurement also provided a supplemental benefit to the investigation in that vertical deflections were measured at the support locations, which were previously assumed to be fixed in this direction.

Structural Identification Using FEMU with DIC Via Hybrid Optimization Algorithm

In a previous study [39], limited non-full-field data derived from DIC measurements were used in an FEMU scheme, but the sparse data used in the refinement was not sufficient for consistent model updating. However, the full-field measurement derived from DIC provided a rational mechanism for performing multi-objective optimization for model updating. In this study, the initial FE models, developed in parallel with the experimental configurations, were updated using a robust optimization algorithm to converge on predictions of the beam's Young's Modulus (E_s) and support stiffness parameters (K_1, K_2, K_3, K_4). As illustrated in Fig. 2, three scenarios were selected for model updating with variations in the restraint conditions and objective function parameters. The optimization algorithm developed in this investigation incorporated the features of a genetic algorithm and a gradient-based scheme to iterate on the unknown parameters.
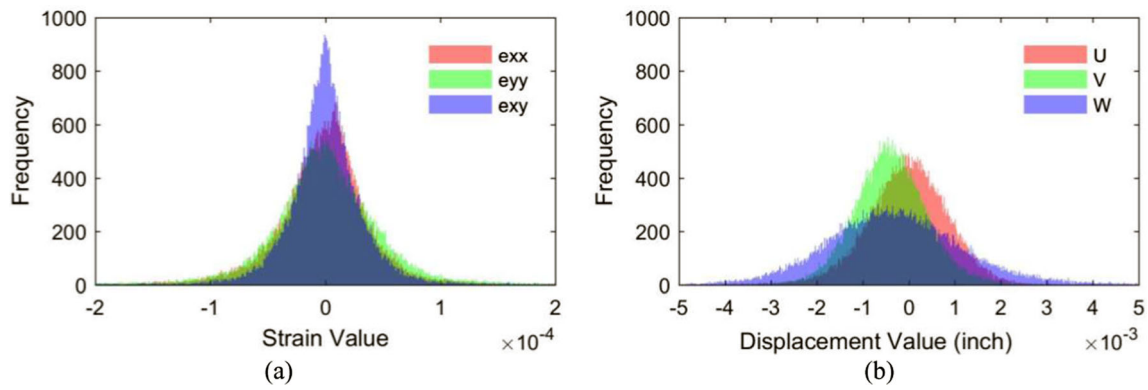
Fig. 7 Histogram of non-zero measurements in a sample zero-load frame (**a**) strain (**b**) displacement

Definition of the objective function

The identification problem consisted of the determination of structural parameters that minimize the difference between calculated data from a numerical model and a set of experimental data. In this research, the numerical model is a finite element model with the same geometry and boundary conditions as the experimental setup. The identification leverages a generalized cost function (e.g. equation (2)) to evaluate agreement between the numerical and experimental results.

$$F = \frac{1}{N_i}|y_i^{num} - y_i^{exp}| \tag{2}$$

Where F is the cost function, y_i^{num} is the i-th information obtained with the numerical simulation, y_i^{exp} is the i-th information obtained with the set of experiments conducted and N_i is a weight factor. In this study, the experimental data utilized for the definition of the cost function are the strain and displacement fields; however, other measurement data could also be included in the St-ID process.
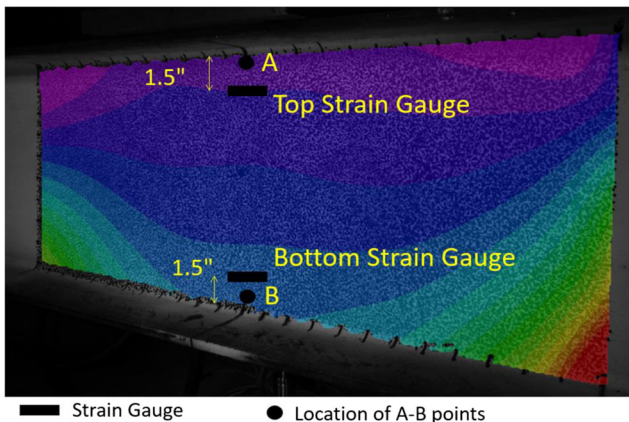

Fig. 8 Longitudinal (ε_{xx}) DIC strain fields at the maximum load, $t = 150$ s, frame#300

Interpolation process

For comparison of the results from these two analyses (e.g. FEM and DIC), a common grid was required to ensure that the measurement/analysis locations are equivalent. To achieve a common reference for comparison between the FEA and DIC results, it was necessary to interpolate the results from the DIC grid over to the FEA grid (or vice versa) or interpolating both results on the new defined mesh grid. In this study, the mapping of both results to a new grid approach was selected. The concept of interpolation process is shown in Fig. 10 schematically. FEA and DIC results have different mesh grid spacing in the x-y plane. With both results mapped to a common grid, the difference (or error) between FEA and DIC results can be used within the optimization process.

In this work, the interpolation was performed using the MATLAB software. For this process a general mesh grid is first defined and the results from FEM and DIC are interpolated onto the newly defined mesh grid. A bilinear interpolation algorithm was developed for this process, where interpolated values of the new grid are obtained based on the values of the four nearest neighbors forming a quad surrounding the interpolated point. Following the alignment of the experimental and numerical results onto a common grid, the final version of the cost function developed in this study can be written as:

$$F = \sum_{i=1}^{480}\sum_{t=100,150,175s}\left(\frac{\left|\varepsilon_{xx}^{num}(i,t)-\varepsilon_{xx}^{exp}(i,t)\right|}{\varepsilon_{xx}^{exp}(i,t)}\right)2$$

$$+ \sum_{i=1}^{480}\sum_{t=100,150,175s}\left(\frac{\left|\varepsilon_{xy}^{num}(i,t)-\varepsilon_{xy}^{exp}(i,t)\right|}{\varepsilon_{xy}^{exp}(i,t)}\right)2$$

$$+ \sum_{i=1}^{480}\sum_{t=100,150,175s}\left(\frac{\left|\delta_{y}^{num}(i,t)-\delta_{y}^{exp}(i,t)\right|}{\delta_{y}^{exp}(i,t)}\right)2 \tag{3}$$

where $\varepsilon_{xx}^{exp}, \varepsilon_{xy}^{exp}$ and δ_{y}^{exp} represent the two components of the strain tensor and displacement, respectively that are
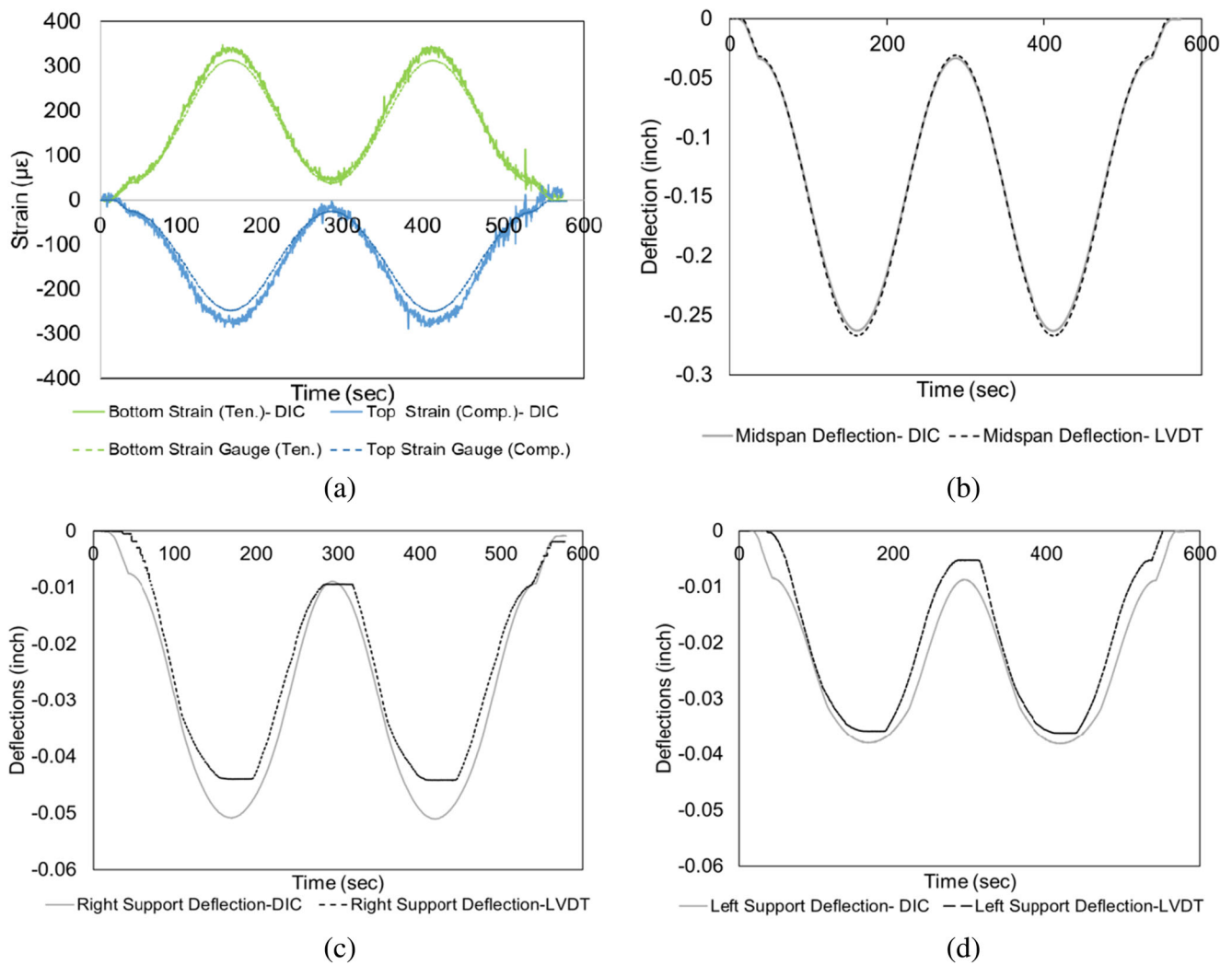
Fig. 9 Comparison of results obtained from DIC and mechanical sensors (**a**) midspan strain; (**b**) midspan deflection; (**c**) right support deflection; (**d**) left support deflection

extracted at a point i of coordinates x_i at time t. The values ε_{xx}^{num}, ε_{xy}^{num} and δ_y^{num} represent the corresponding values computed from the finite element model. In this study, the data for three representative time frames, namely $t = 100$, 150, 175 s., were selected to be included in the cost function to provide a representation of different stages of loading while maintaining a reasonable computational cost.

Optimization process- Hybrid Genetic Algorithm (HGA)

In this study a hybridized training algorithm was adopted to minimize the cost function (equation (3)) and derive unknown parameters (E_s, K_1, K_2, K_3, K_4). The algorithm was based on the combination of a Genetic Algorithm (GA) and a gradient-based algorithm. Both GA and gradient-based techniques are well-established optimization methods and have been used in

Table 2 Differences between DIC and LVDT

Differences between DIC and LVDT	Top strain	Bottom strain	Midspan deflection	Right support deflection	Left support deflection
Mean absolute percentage difference: $MAPE = \frac{100}{n}\sum_{t=1}^{n}\left|\frac{100}{n}\right|$ (%)	6.4	5.4	1.2	12.5	11.5
Maximum difference: $\|y_{DIC} - y_{sensor}\|$ (μs) & (in.)	23	22	0.004	0.007	0.002

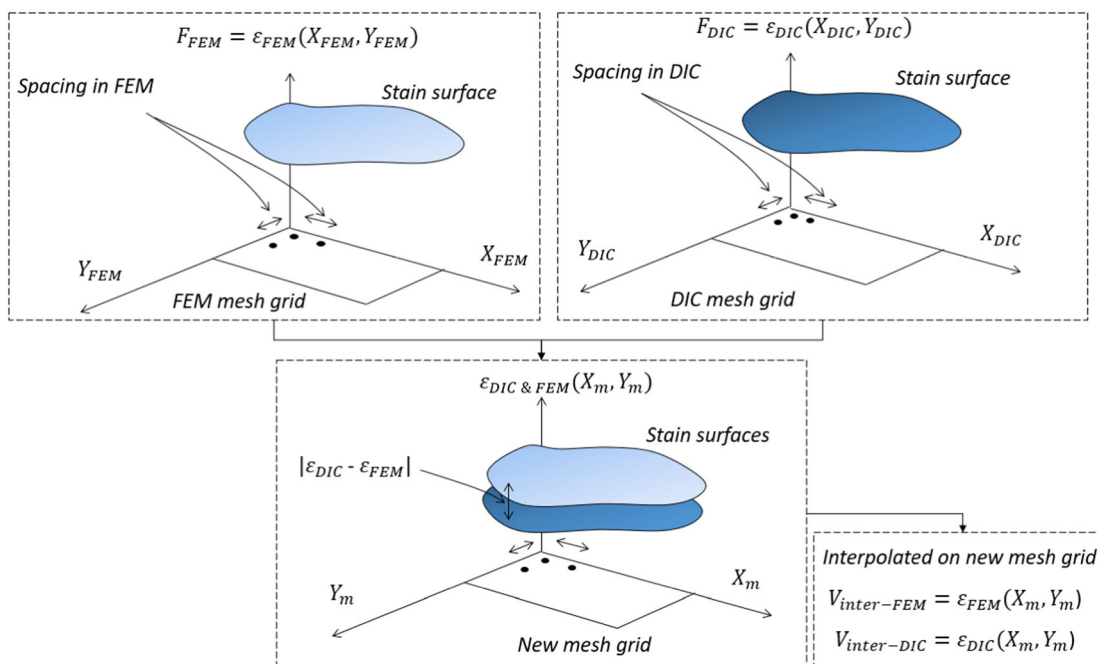*($e_t = y_{DIC} - y_{sensor}$, n = number of measured data)*

Fig. 10 Interpolation process

numerous optimization problems [40]; however, previous literature has shown that in problems involving a large number of parameters, a combination of these two techniques yields superior optimization performance [36].

In the selected Hybrid Genetic Algorithm (HGA), first a genetic optimization step is employed to explore the space of parameters and locate the approximate region of the optimum solution. In the second step, a gradient-based method is utilized to continue the search within the approximate region to quickly converge on the precise location of the optimum solution. As a result, the favorable characteristics of both methods namely the efficient exploration of the space by the GA and the superior convergence of the gradient-based methods are leveraged to achieve an efficient optimization. Figure 11 illustrates a basic flowchart of the HGA procedure adopted in this work. As shown, a feasible initial guess for the parameters is used to start the process. The initial guess is used to generate an FEA model which upon analysis will be evaluated in the cost function. If the stopping criteria are not met, a new solution is generated through different operations in GA (e.g. selective reproduction, crossover and mutation). The new solution gives rise to a new FEA model and the process will be repeated as necessary. Once the stopping criteria are satisfied, the final solution of GA will be used to initiate the gradient-based scheme. This step will continue until convergence criteria are satisfied when the final optimal solution is identified.

Table 3 shows the initial values selected within the feasible range (maximum and minimum values) used as the initial guess for the parameters in the HGA procedure. Before the

updating process, an initial model was created based on the initial values shown in Table 3. Table 4 presents three representative sets of training parameters to be used within the GA based on literature [40–42]. For the parameters used in the algorithm, N_{pop} represents the initial population, N_{elites} represents population of elites which go directly to the next generation, N_{mut} represents the population which are randomly selected for mutation, μ represents the probability rate of mutation, N_{pairs} represents the selecting parents for mating, and *iterations* describe stopping criteria for termination. It should be noted that optimization process represents a trade-off between computational time and solution accuracy and that the parameters selected in this study only represent three optimization scenarios aimed toward validity of the approach rather than convergence to the exact solution.

Solution convergence

Configuration 1 (CF1) was used to evaluate the performance and efficiency of the parameter groups presented in Table 4. In this context, performance was described as the capability to converge to a rational solution of E_s (assumed to be 29,000 ksi) at the global minima, with efficiency described by the time of solution. An illustration of the solution efficiency is shown in Fig. 12, which highlights the evolution of the cost function as the parameters converge towards their optimal solution. As seen in this figure, the GA training was stopped in each case at 20 epochs where an obvious plateau would be reached in the cost function and the parameters. At this point, the gradient-based algorithm was initiated which further
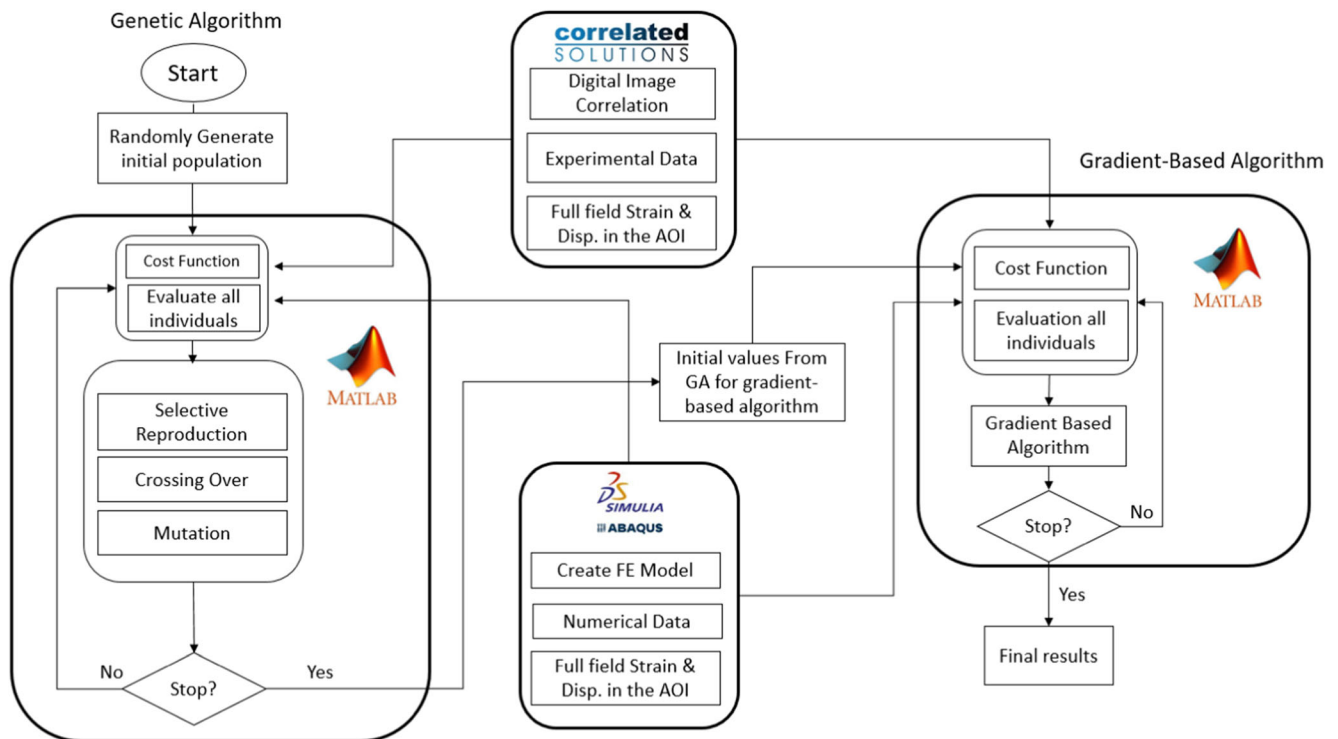
Fig. 11 Overview of the proposed hybrid-genetic algorithm

minimized the cost function and resulted in the final convergence. Table 5 includes the parameter results of the optimization solutions for this configuration. The results demonstrate that *CF1B* and *CF1C* both exhibit satisfactory performance when compared to *CF1A*, but the computational cost for *CF1C* is much higher without a significant improvement in performance. *CF1A* does not approach a rational solution for E_s and appears to be stuck at some local minima, highlighting the importance of the number of individuals (N_{pop}) used in the first generation of the hybrid-optimization algorithm. Our rationale for selecting the parameter group B was based primarily on solution time (or computational cost) along with the convergence outcome for the one parameter with a generally well-known value, modulus of elasticity E_s. Future studies on this topic will explore the selection of optional parameters.

As noted convergence for each of the final parameter selections manifested as a plateau in each parameter. For the modulus of elasticity parameter, the rational solution for steel provided a reference for comparison; however, for the restraint conditions no such comparison was available. To evaluate the final parameters for the boundary restraints a convergence study was performed to correlate the degree of model restraint relative to the idealized solution. For the pin-roller condition, the expectation was zero rotational restraint and infinite vertical restraint, whereas the expectation for the fixed condition maintained that same vertical restraint, but included infinite rotational restraint.

The parametric study used for both types of boundary conditions were based on the assumption that for full restraint (either vertical or rotational), the displacement or rotations would converge to a value of zero (or near zero). For the displacement, this hypothesis was tested in the FEA model by selecting a target value in a displacement-controlled analysis (i.e. 0.3 in) and evaluating the model response with varying restraint stiffness values. For the vertical support springs, this initially resulted in the springs deforming and the midspan displacement not reaching the 0.3 threshold. This process was iterated until a plateau was reached in the midspan displacement (which was the threshold value selected). This plateau was assumed to represent full vertical restraint. This value was considered 100% fixity and all other values (%) were determined relative to this maximum. A similar approach was used

Table 3 Initial, minimum and maximum values of the updating parameters	Material parameter	E_s (ksi)	K_1 (lb/in.)	K_2 (lb/in.)	K_3 (Kip in./rad)	K_4 (Kip in./rad)
	Initial	25,000	70,000	70,000	2000	2000
	min	20,000	50,000	50,000	50	50
	max	40,000	1,500,000	1,500,000	500,000	500,000

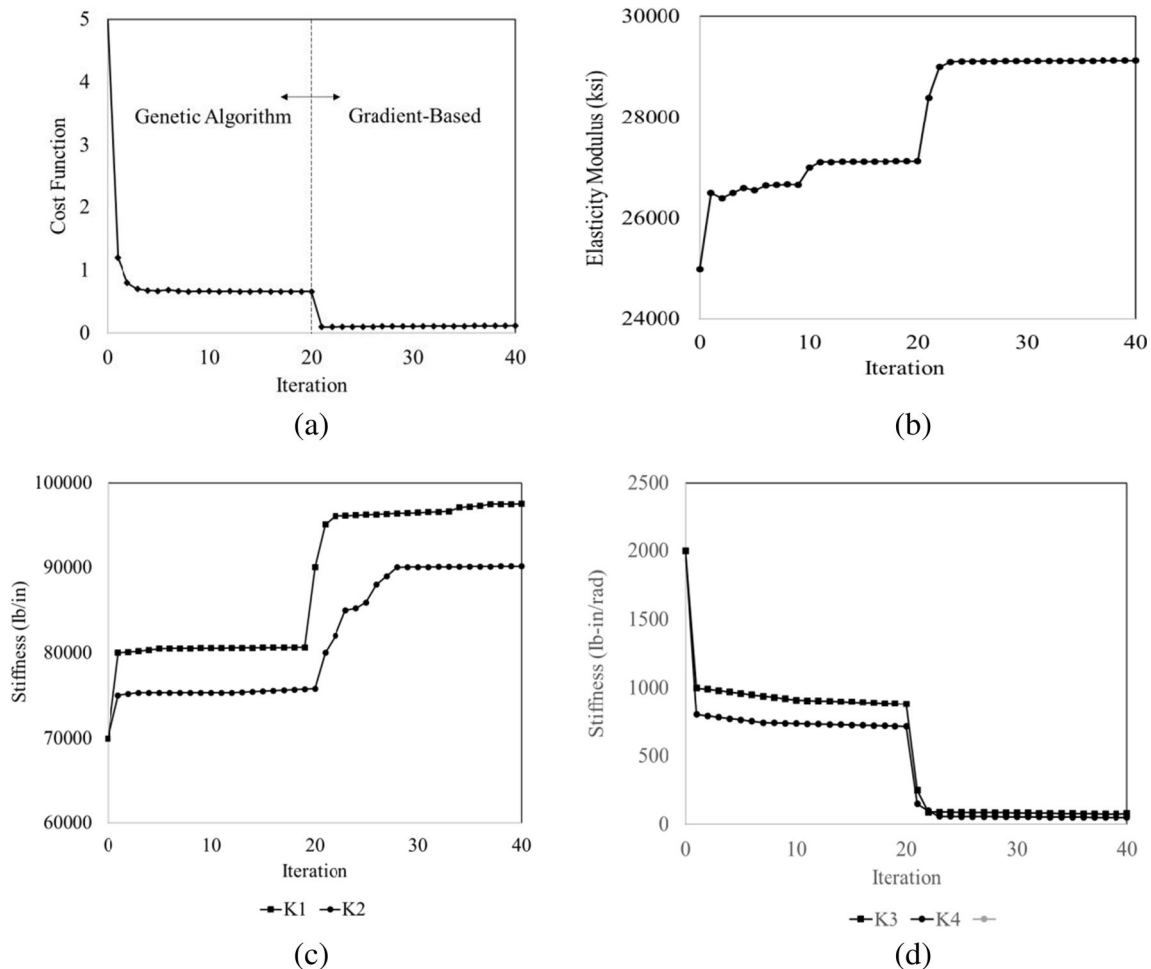**Table 4** Parameters of the genetic algorithm (GA) for the three identification tests for the first configuration

GA Parameter Group (PG)	N_{pop}	N_{elites}	N_{mut}	μ	N_{pairs}	Iterations
A	10	1	2	0.04	7	40
B	20	2	4	0.04	14	20
C	50	4	8	0.04	28	20

for the rotational restraint, but the threshold used was the end rotation value, which was assumed to converge to zero for full fixity.

The convergence study used the finite element model of the test beam with the boundary restraint stiffnesses parameterized. Using the model, the values of the boundary restraints (e.g. K_1/K_2 and K_3/K_4) were varied iteratively to establish the upper and lower bounds of the restraint stiffness required to mimic the idealized solutions (i.e. simple and fixed conditions). This idealized solution is realized when the selected degree of freedom converges to a plateau, indicating additional restraint stiffness does not yield additional restraint

resistance. The resulting convergence study demonstrated that a fixed vertical restraint stiffness equates to 250,000 lb./in, whereas full rotational restraint equates to 500,000 Kip in./rad. For the configurations evaluated in this study, Fig. 13 illustrates the evolution of restraint as the vertical and rotational restraints approach the idealized solutions. Also Fig. 14 illustrate the evolution of rotational restraint values which is acquired by selecting different values for rotational spring stiffness of one of the supports and then analyzing the beam using ABAQUS to obtain the evolution of support rotation values.

When comparing the updated restraint stiffness values, it is evident that the boundary conditions of the three configurations represent some fraction of the idealized boundary conditions (0.016% for configurations 1 and 2, and 0.04% for configuration 3). This level of rotational fixity was expected for the first two configurations which were designed to be rotationally unrestrained. However, for configuration 3, this percentage, while larger than the two unrestrained configurations, is much lower than expected (Fig. 13(a)). This demonstrates the inefficiency of the designed clamping system in creating rotational fixity. Upon further examination, it was


Fig. 12 Evolution of unknown parameter convergence versus iterations for CF1B (**a**) Cost Function (**b**) Modulus of Elasticity (**c**) K_1, K_2 (**d**) K_3, K_4

Table 5 Identified optimal parameters based on Hybrid Genetic Algorithm for different parameters of the GA for the first configuration

Configuration/ Parameter group	E_s (ksi)	K_1 (lb/in.)	K_2 (lb/in.)	K_3 (Kip in./rad)	K_4 (Kip in./rad)	Solution time (Hour)
CF1A	27,488	92,551	90,165	125	188	20
CF1B	29,100	97,416	90,020	80	54	20
CF1C	29,244	98,018	88,000	55	66	50
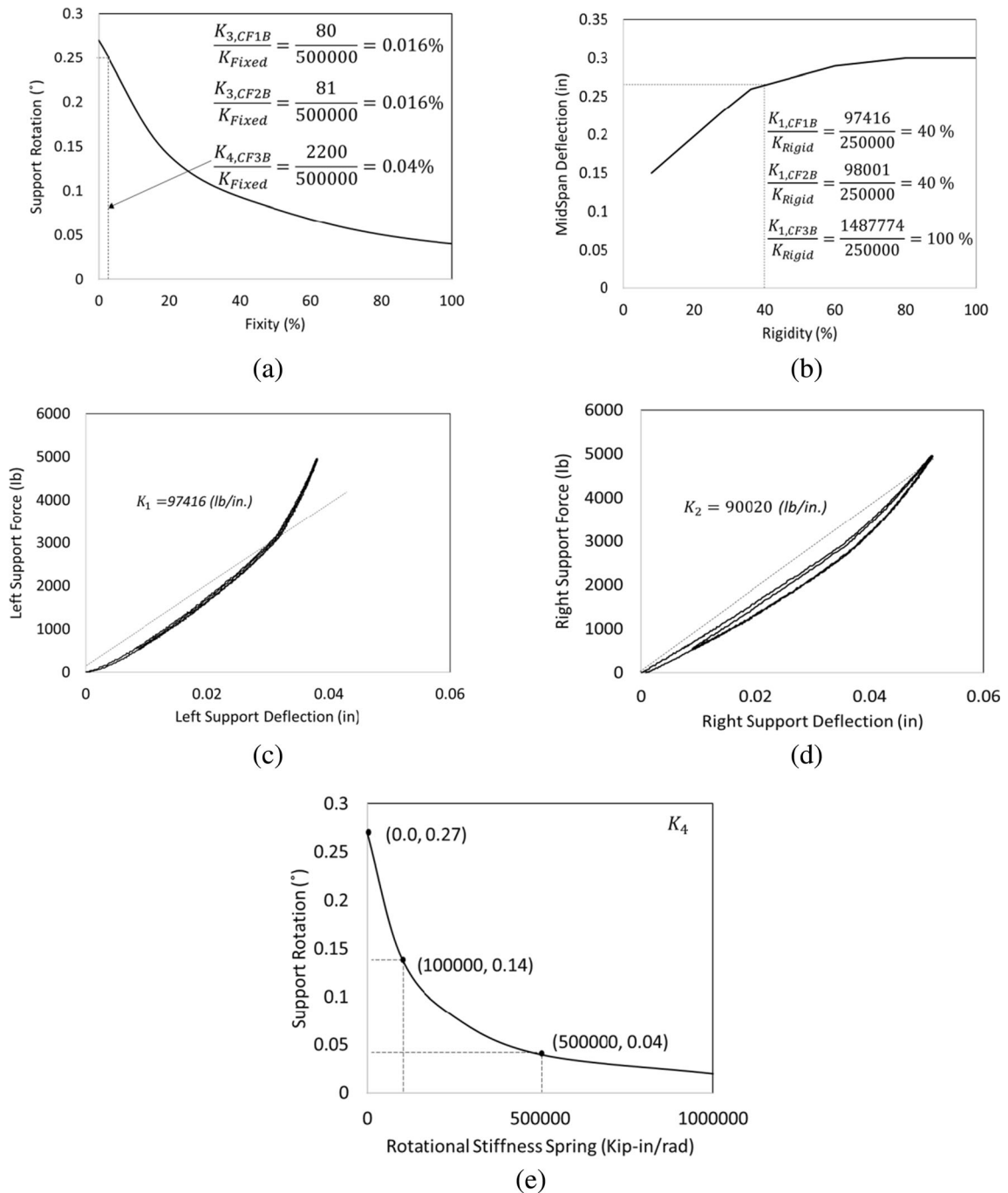
Fig. 13 Convergence study on restraint stiffness (**a**) evolution of rotational restraint fixity of the supports (**b**) evolution of vertical restraint rigidity of supports (**c**) force versus left support deflection (**d**) force versus right support deflection (**e**) Rotational Stiffness Spring versus Support Rotation obtained from ABAQUS

Fig. 14 Rotational spring stiffness variance versus degree of rotations
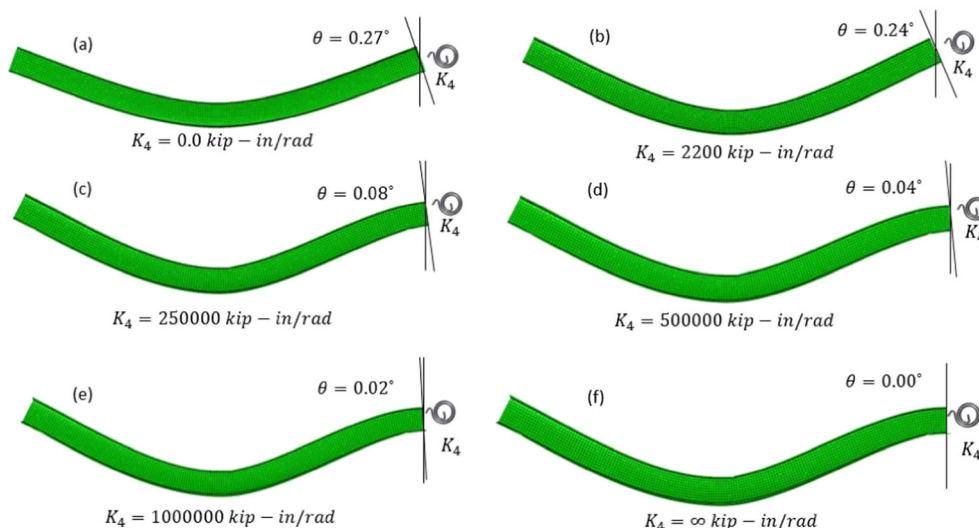
noted that the clamping device used in this configuration acted on a limited length (4 in.) of only the lower flange and was thus not able to effectively restrain the rotation of the beam end. A more robust mechanism for fixing the ends of both top and bottom flange over a sufficient length will be required for creating an actual rotationally fixed support conditions.

Similarly, for the vertical spring stiffness (K_1 and K_2), the updated stiffness values are approximately 40% of the expected vertical restraint (Fig. 13(b)). The reduction for the vertical restraint was attributed to the support deformation that occurred during the early stages of loading due minor gaps or spacing in the pedestals and associated fixtures. The support movement dissipated at approximately 86% of the peak load, which is illustrated in the load deflection response of the supports (Fig. 13(c) and (d)), the slope of which correlates to the average support vertical restraint stiffness (K_1 and K_2).

In Fig. 13(c), (d): Left and Right support force-deflections are quite nonlinear (but elastic). As these values of reported stiffness are a representative average. This turned out to be a by-product of the experimental setup and could not be easily controlled. Consideration was given to starting the analysis after the point of support stiffening, but it was decided to include this effect in the model updating process for illustrative purposes.

In Fig. 13(e), the evolution of rotational stiffness spring versus support rotation values, obtained from ABAQUS, is plotted for the purpose of knowing how we have selected maximum rotational spring stiffness domain for the optimization process appropriately. As it can be seen in Fig. 13(e), beyond a support restraint stiffness of 500,000 Kip-in/rad,

little difference are observed within the support rotation values. Importantly, it has to be noted that in the optimization process if a large domain for the unknown parameters is selected, such as the rotational spring stiffness, poor parameter estimates are likely unless a large population for the GA is selected, which in turn would increase computational cost. Owing to that, selection of the domain of the parameters must be done with consideration of these tradeoffs. This concept is shown in Fig. 13(e), in which an initial and maximum range for the rotational spring stiffness were chosen accordingly. In future works, the sensitivity of optimization parameters such as population size will be studied in more depth.

With the rationality of the optimized parameters established, it was determined that the parameter group B yielded the most efficient optimization solution and was selected for evaluation of the other two configurations (CF2 and CF3). Using this parameter group, the final identified parameters are presented in Table 6 for all three test configurations.

A comparison between the full-field contours of the DIC and the updated FE model are presented in Figs. 15 and 16 for the midspan and support locations, respectively for CF1B. Figure 15 illustrates a comparison of the longitudinal strain (ε_{xx}), shear strain (ε_{xy}), and vertical deflection (δ_y). From this comparison, it is evident that the updated model is able to reproduce the responses derived from the experiment as illustrated by the minimal error exhibited within the area of interest. It should be noted that the localized errors in the longitudinal strain contours are likely associated with local stress concentrations that occur on the top of the beam at the location

Table 6 Identified optimal parameters for different configurations for group B set of parameters of the GA

| Configuration/ Parameter group	E_s (ksi)	K_1 (lb/in.)	K_2 (lb/in.)	K_3 (Kip in./rad)	K_4 (Kip in./rad)
CF1B	29,100	97,416	90,020	80	54
CF2B	29,511	97,501	91,888	48	101
CF3B	29,984	1,568,698	1,384,224	249	2200
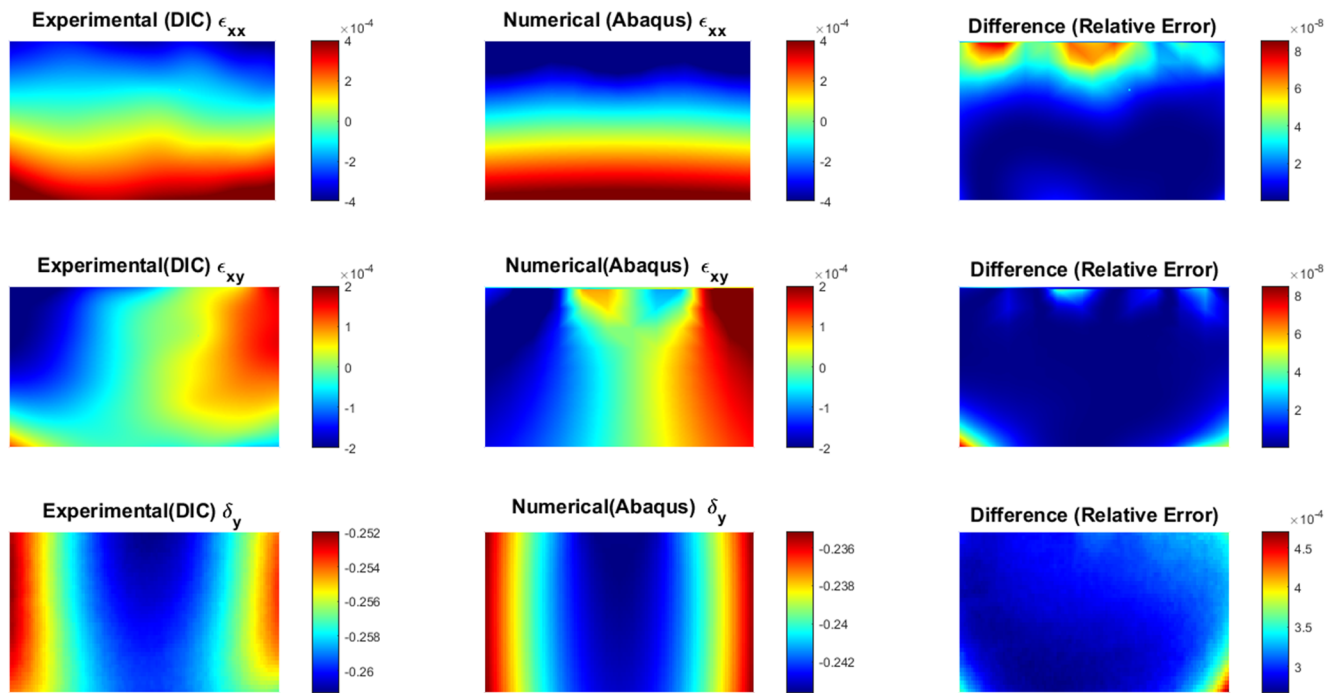
Fig. 15 Contour plots of the experimental strain fields, the numerical strain fields and their absolute difference for the middle span for the components ε_{xx}, ε_{xy},δ_y at $t = 150$ s for CF1B

of the load application. Figure 16 illustrates a comparison of the deflections at the end locations showing excellent agreement. It is also notable that while the vertical deflection right above the supports were initially expected to be zero, some support settlement can be seen in the results. Similar to the midspan location, the error between the DIC measurement and updated model is minimal across the area of interest. Similar results were derived for *CF2B* and *CF3B*, but are not included in this manuscript.

Performance of Updated FE Model

To investigate the effectiveness of the identification procedure, the performance of the model before and after updating can be evaluated versus the results derived from the experiments. For this evaluation, two points of interest for *CF1B* were selected for comparison, namely points A and B which were previously described in Fig. 8. The temporal evolution of the longitudinal strain both before and after the updating
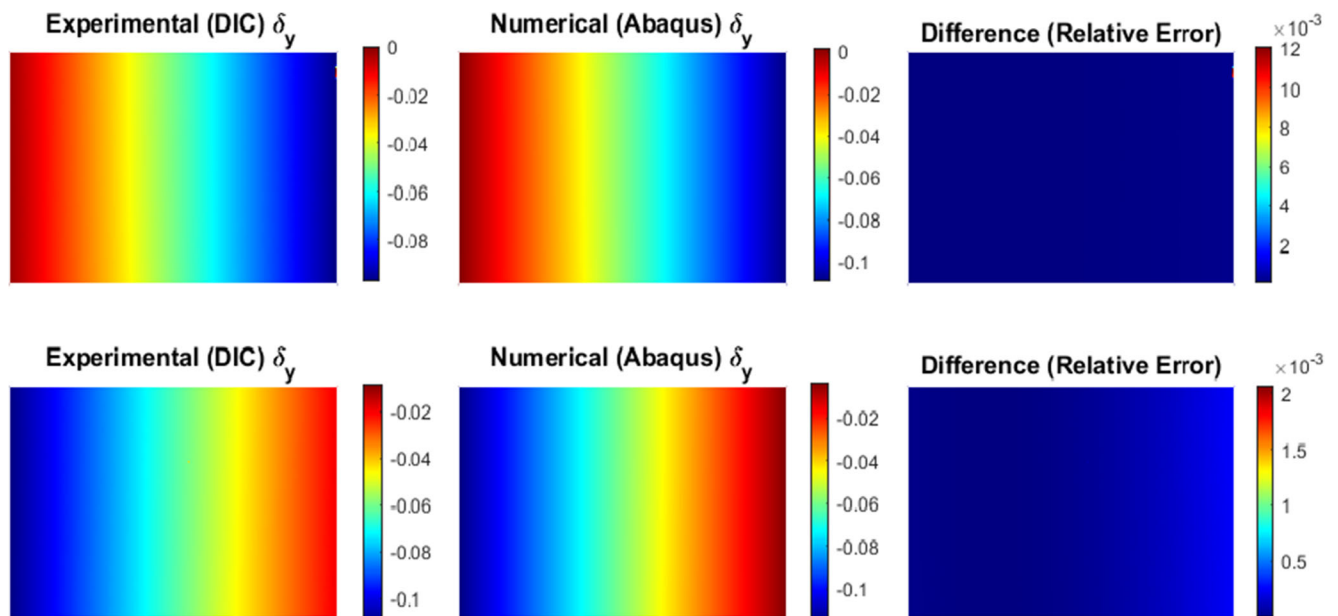
Fig. 16 Contour plots of the experimental strain fields, the numerical strain fields and their absolute difference for the component δ_y (first row for left span and second row for right span) at t = 150 s for CF1B
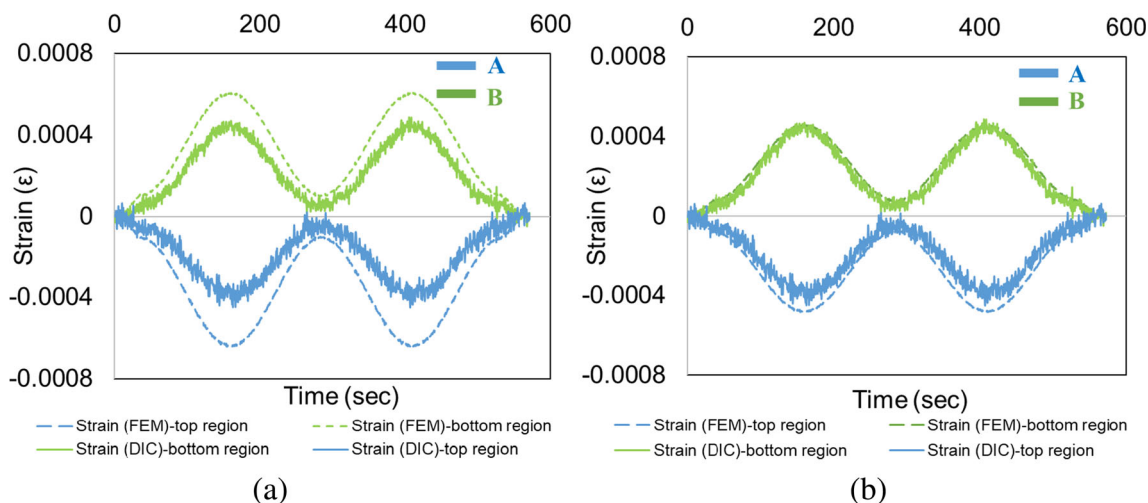
Fig. 17 Comparison of the evolution of the longitudinal strains ε_{xx} for CFB1 between the numerically computed values and the values obtained using DIC at points A-B shown in Fig. 8, for (**a**) before model updating, (**b**) after updating

process are shown in Fig. 17(a) and (b), respectively. Also, a summary of the percent difference, described as the mean absolute percentage error (MAPE) between DIC and FEM, for the three configurations before and after model updating, are presented in Table 7. Comparing the results from the updated model with those derived from the DIC measurements demonstrate the success of the identification procedure, in that the revised strain response now tracks along with those derived from the experiment. It is seen that the evolution of local strain is correctly described over the entire loading sequence, with comparable magnitudes and falls within about an 8% error window of the measured response. Similar results were derived for *CF2B* and *CF3B*, but are not included in this manuscript. This outcome demonstrates that full-field measurement techniques are sufficiently robust for use in the St-ID framework for SHM.

Conclusion

In this study, a structural identification procedure was developed to identify the material properties and boundary conditions of the experimental setup of a steel beam under flexural loads using full field measurements derived from 3D digital image correlation (3D-DIC). This paper describes the core

components of the St-ID process including the experimental setup, numerical model development, creation of common reference plane, and model updating. Conventional mechanical sensors typically used in St-ID applications were also installed on the experimental specimen to provide context for comparison with the current practice. In this work, both deflections and local strain fields were successfully used in the updating procedure through the deployment of a cost function that included the relevant components of full-field structural response in a number of different stages of loading. This cost function was then pushed to zero by leveraging an efficient optimization algorithm consisting of a hybrid of genetic algorithm (GA) and a gradient-based optimizer.

A number of different optimization parameters were tested and compared in terms of convergence performance as well as computational efficiency. The examination of the evolution of the cost function as well as the identified parameters versus time demonstrated satisfactory convergence. The excellent agreement of the strain and displacement responses achieved after the completion of the updating process confirmed the efficacy of the proposed identification method. It was also observed that while the responses obtained through DIC were relatively noisier than the physical sensors, the full-field measurement provided a rich dataset for a stable and robust structural identification. Overall, the St-ID results obtained in this

Table 7 Summary of differences between DIC and FEM before and after model updating for the mentioned points

		Before model updating (BMU)		After model updating (AMU)	
		Top strain (A)	Bottom strain (B)	Top strain (A)	Bottom strain (B)
Mean absolute percentage error: $MAPE = \frac{100\%}{n}\sum_{t=1}^{n}\left|\frac{100\%}{n}\right|(\%)$	Configuration 1	35	24	8	3
	Configuration 2	38	22	12	5
	Configuration 3	32	17	7	6

e_t, $y_{\text{BMU}} - y_{AMU}$; *n, number of measured data*)

work suggest that image-based measurements sensing using 3D-DIC can be successfully used as an alternative to physical in-place sensors for characterizing the response of large scale structural systems.

Future work is expected to further explore the potential for reducing the noise within the experiments, optimal parameter selection for the parameter identification, evaluation of the range of applicability with respect to uncertainty in the updated parameters and applying different boundary condition configurations to demonstrate the capability of the proposed approach. These areas of focus are critical to the applicability of the proposed approach to more complex structural systems.

References

1. American Society of Civil Engineers (ASCE) (2017) Report card for America's Infrastructure. https://www.infrastructurereportcard.org/. Accessed May 2017

2. Wardhana K, Hadipriono FC (2003) Analysis of recent bridge failures in the United States. J Perform Constr Facil 17(3):144–150

3. Graybeal BA, Phares BM, Rolander DD, Moore M, Washer G (2002) Visual inspection of highway bridges. J Nondestruct Eval 21(3):67–83

4. Sohn H, Farrar CR, Hemez F, Czarnecki J (2004) A review of structural health monitoring literature: 1996–2001. Los Alamos National Laboratory, Los Alamos

5. Aktan AE, Catbas FN, Grimmelsman KA, Tsikos CJ (2000) Issues in infrastructure health monitoring for management. J Eng Mech 126(7):711–724

6. Ahlborn TM, Shuchman R, Sutter LL, Brooks CN, Harris DK, Burns JW, Endsley KA, Evans DC, Vaghefi K, Oats RC (2010) The state-of-the-practice of modern structural health monitoring for bridges: a comprehensive review. Department of Civil and Environmental Engineering, Michigan Tech Transportation Institute, Michigan Technological University, Accession number: 01338807, Contract number: DTOS59-10-H-00001

7. Vaghefi K, Oats RC, Harris DK, Ahlborn TM, Brooks CN, Endsley KA, Roussi C, Shuchman R, Burns JW, Dobson R (2012) Evaluation of commercially available remote sensors for highway bridge condition assessment. J Bridg Eng 17(6):886–895

8. Webb GT, Vardanega PJ, Middleton CR (2014) Categories of SHM deployments: Technologies and capabilities. J Bridg Eng 20(11): 04014118

9. Noel AB, Elfouly T, Badawy A (2017) Structural health monitoring using wireless sensor networks: a comprehensive survey. IEEE Commun Surv Tutorials 19(3):1403–1423

10. Al-Radaideh A, Al-Ali AR, Bheiry S, Alawnah S (2015) A wireless sensor network monitoring system for highway bridges. 1st International Conference on Electrical and Information Technologies ICEIT'2015

11. Hu X, Wang B, Ji H (2013) A wireless sensor network-based structural health monitoring system for highway bridges. Comput-Aided Civ Inf Eng 28:193–209

12. Bartoli G, Facchini L, Pieraccini M, Fratini M, Atzeni C (2008) Experimental utilization of interferometric radar techniques for structural monitoring. Struct Control Health Monit 15(3):283–298

13. Doebling SW, Farrar CR, Prime MB (1998) Summary review of vibration-based damage identification methods. Shock Vib Dig 30(2):91–105

14. Ribeirio D, Calcada R, Delgado R, Brehm M, Zabel V (2012) Finite element model updating of a bowstring-arch railway bridge based on experimental modal parameters. Eng Struct 40(7):413–435

15. Friswell MI, Mottershead JE (1995) Finite element model updating in structural dynamics. Kluwer Academic Publishers, London Sections 3.7, 7.4

16. Correlated Solutions Inc. (2005) VIC-3D user manual. Correlated Solutions, Columbia

17. "MatchID," [Online]. Available: http://www.matchidmbc.com/

18. Pan B (2010) Recent progress in digital image correlation. Ex Mech 51:1223–1235

19. Blaber J, Adair B, Antoniou A (2015) Ncorr: open-source 2D digital image correlation MATLAB software. Exp Mech 55(6):1105–1122

20. Cheng P, Sutton MA, Schreier HW, McNeill SR (2002) Full-field speckle pattern image correlation with B-spline deformation function. Exp Mech 42:344–352

21. Pan B, Li K, Tong W (2013) Fast, robust and accurate digital image correlation calculation without redundant computation. Exp Mech 53:1277–1289

22. Hild F, Roux S (2011) Comparison of local and global approaches to digital image correlation. Ex Mech 52:1503–1519

23. Bornert M, Bremand F, Doumalin P, Dupre JC, Fazzini M, Grediac M, Hild F, Roux S, Mistou S, Molimard J, Orteu JJ, Robert L, Surrel P, Vacher Y, Wattrisse B (2009) Assessment of digital image correlation measurement errors: methodology and results. Ex Mech 49:353–370

24. Cheng P, Sutton MA, Schreier HW, McNeill SR (2002) Fullfield speckle pattern image correlation with b-spline defromation function. Ex Mech 42:344–352

25. Crammond G, Boyd S, Dulieu-Barton J (2013) Speckle pattern quality assessment for digital image correlation. Opt Lasers Eng 51(12):1368–1378

26. Lionello G, Cristofolini L (2014) A practical approach to optimizing the preparation of speckle patterns for digital-image correlation. Meas Sci Technol 25(10):107001

27. Ke XD, Schreier HW, Sutton MA, Wang YQ (2011) Error assessment in stereo-based deformation measurements-part II: Experimental validation of uncertainty and bias estimates. Exp Mech 51(4):423–441

28. Kahn-Jetter ZL, Chu TC (1990) Three-dimensional displacement measurements using digital image correlation and photogrammic analysis. Exp Mech 30(1):10–16

29. Pan B, Qian KM, Xie HM, Asundi A (2009) Two-dimensional digital image correlation for in-plane displacement and strain measurement: a review. Meas Sci Technol 20(6):062001 17pp

30. Hild F, Roux S (2006) Digital image correlation: from displacement measurement to identification of elastic properties – a review. Strain 42(2):69–80

31. Chen F, Chen X, Xie X, Feng X, Yang L (2013) Full-field 3D measurement using multi-camera digital image correlation system. Opt Lasers Eng 51(9):1044–1052

32. Zapico JL, Gonzalez MP, Friswell MI, Taylor CA, Crewe AJ (2003) Finite element model updating of small scale bridge. J Sound Vib 268:993–1012

33. Schlune H, Plos M, Gylltoft K (2009) Improved bridge evaluation through finite element model updating using static and dynamic measurements. Eng Struct 31(7):1477–1485

34. Sanayei M, Phelps JE, Sipple JD, Bell ES, Brenner BR (2012) Instrumentation, non-destructive testing, and finite element model updating for bridge evaluation using strain measurements. J Bridg Eng 17(1):130–138

35. Okasha NM, Frangopol DM, Orcesi AD (2012) Automated finite element updating using strain data for the lifetime reliability assessment of bridges. Reliab Eng Syst Saf 99:139–150

36. Jung DS, Kim CY (2013) Finite element model updating of a simply supported skewed PSC I-girder bridge using hybrid genetic algorithm. KSCE J Civ Eng 17(3):518–529

37. Manual of steel construction. Load and resistance factor design, third edition. Copyright 2001 by American Institute of Steel Construction, Inc. ISBN 1–56424–051-7

38. Wang ZY, Li HQ, Tong JW, Ruan JT (2007) Statistical analysis of the effect of intensity pattern noise on the displacement measurement precision of digital image correlation using self-correlated images. Exp Mech 47(5):701–707

39. Shafiei Dizaji M, Alipour M, Harris D (2016) Leveraging vision for structural identification – a digital image correlation based approach. International Digital Image Correlation Society Conference (iDICs), SEM fall conference, November 8–11, Philadelphia, PA, US

40. Goldberg DE (1989) Genetic algorithm in search, optimization and machine learning. Addison-Wesley, Reading

41. Joghataie A, Farrokh M (2008) Dynamic analysis of non-linear frames by Prandtl neural networks. J Eng Mech 134(11):961–969

42. Farrokh M, Shafiei Dizaji M, Joghataie A (2015) Modeling hysteretic deteriorating behavior using generalized Prandtl neural network. J Eng Mech 141(8):040150